Solar RRL
www.solar-rrl.com

Silver Metallization with Controlled Etch Stop Using SiO_x Layers in Passivating Contacts for Improved Silicon Solar Cell Performance

Raphael Glatthaar, Franz-Philipp Schmidt, Adnan Hammud, Thomas Lunkenbein, Tobias Okker, Frank Huster, Sven Seren, Beatriz Cela Greven, Giso Hahn, and Barbara Terheiden*

Metallization of polycrystalline-silicon/silicon oxide (poly-Si/SiO_x) passivating contacts with fire-through silver paste is a crucial process for implementation of passivating contacts in industrial manufacturing of solar cells. For a microscopic understanding of the metallization process, the contact forming interface between the Ag crystallites and the poly-Si layer is investigated with high-resolution transmission electron microscopy. For this purpose, multilayer atmospheric pressure chemical vapor deposition poly-Si samples with a SiO_x layer between the individual poly-Si layers are fabricated, screen printed with a lead-free Ag paste, and contact fired. Electron micrographs show that in this process the etching of the paste and the subsequent Ag crystallite formation is stopped by this interface with the SiO_x layer. Additionally, energy-dispersive X-Ray mapping reveals the presence of an oxide layer around the Ag crystallites. This finding differs significantly from well-investigated classical cell concepts with contact formation on diffused crystalline silicon. Moreover, an analysis of the Ag crystallite orientation in correlation to the neighboring Si crystallite orientation indicates no direct relationship. Finally, it is shown that the use of this multilayer approach is favorable for integration into a solar cell concept leading to a higher passivation quality at the metallized area and lower contact resistivity.

1. Introduction

Crystalline silicon (c-Si)-based solar cells are by far the dominating photovoltaic (PV) technology and have recently shown outstanding efficiencies approaching the thermodynamic limit with heterojunctions and passivating contact solar cell concepts.[1–3] The success in global PV production did not happen only due to the constant increase in efficiency, but above all due to the cost reduction of the industrial fabrication processes used. Currently, industrial fabrication starts the shift from cells with diffused surfaces to advanced cell concepts as, for example, passivating front and/or back contacts or even with interdigitated back contacts (IBC).[4] A hurdle is the metallization process, which is carried out ideally using the highly optimized screen-printing process of metal pastes. The knowledge about this contact formation of a fire-through Ag paste for classical, diffused c-Si cells has become very detailed due to numerous investigations in the past years (e.g.,[5–9]). To the best of the authors' knowledge, however, there are no specific contact formation models available of contacting poly-Si/SiO_x layer stacks by a fire-through Ag paste. With this article, we aim to close this lack of knowledge and, in particular, highlight the fundamental differences. Since basic mechanisms of contact formation are similar to the classical case, we first summarize the current state of knowledge about the contact formation of a fire-through Ag paste.

A detailed model of contact formation was summarized by Schubert,[10] then further elaborated and extended by others,[6–9] and describes a paste that consists largely of Ag particles. In

R. Glatthaar, T. Okker, F. Huster, G. Hahn, B. Terheiden
Department of Physics
University of Konstanz
Universitätsstr. 10, 78464 Konstanz, Germany
E-mail: raphael.glatthaar@uni-konstanz.de

The ORCID identification number(s) for the author(s) of this article can be found under https://doi.org/10.1002/solr.202300491.

DOI: 10.1002/solr.202300491

F.-P. Schmidt, A. Hammud, T. Lunkenbein
Department Inorganic Chemistry
Fritz-Haber-Institut of the Max-Planck Society
Faradayweg 4-6, 14195 Berlin, Germany

S. Seren
Research and Development Department
SCHMID Group
Robert-Bosch-Str 32-36, 72250 Freudenstadt, Germany

B. Cela Greven
Technology Department
Fenzi AGT
Fregatweg 38, 6222 NZ Maastricht, Netherlands

addition to organic material and solvents, which are required for the technical implementation of screen printing, there is also the so-called glass frit component. Formerly, one of the important components was PbO; nowadays, glass frits are based on TeO_2 as the main material, which is more environmentally friendly. Starting from temperatures of 500–650 °C in the fast firing process, this component softens and etches the SiN_x layer, which serves as a surface passivation and antireflection coating.[7] Apart from the etching process caused by the glass frit, which can etch besides the SiN_x and also the Si itself, another etching process dominates at higher temperatures.[6,7] Therefore, Ag ions from the Ag particles are dissolved in the fluidized phase and migrate to the silicon surface and etch there with following reaction.

$$(Ag^{+} + 2\,O^{2}\ ) + Si \rightarrow Ag + SiO_2 \quad (1)$$

Due to the different atomic packing factors of the lattice planes, c-Si substrates with {100} surfaces are etched anisotropically, resulting in inverted pyramids. During cool down, the Ag atoms precipitate and grow with an epitaxial relationship to the {111} Si planes and refill these inverted pyramidal structures.[8,11,12] These Ag crystallites then enable an electrical contact between the c-Si and the metal finger. The charge carrier transport from these Ag crystallites to the bulk Ag finger is then possible via different current paths. Since this probably depends in detail on the metallization system used, many dominant current paths have been presented in the past. Besides direct Ag crystallite/Ag bulk contacts,[9,10] there are current paths through the thin glass layer[10,13] and multistep tunneling through Ag nanocolloids or other highly conductive nanoparticles in the glass layer.[11,14]

The charge carrier transport from the Ag crystallites to the Ag bulk is likely to be the same in other cell concepts such as the passivating contacts. In contrast, the Ag crystallite formation and thus the charge carrier transport from the Si (c-Si and poly-Si) to the Ag crystallite are shown to be different in the poly-Si/SiO_x structures.[15] Scanning electron microscopy (SEM) images of recently published investigations show that the poly-Si morphology, and more importantly the poly-Si/SiO_x interface, impedes the Ag paste etching process and thus consequently the resulting Ag crystallite growth into the underlying Si base substrate.[15–18] This is especially true for planar surfaces where Ag crystallites rarely penetrate the c-Si base substrate. On textured surfaces Ag grows to larger crystallites and massive etching into the base substrate is commonly observed at pyramid tips and edges.[19,20] The stopping mechanism of the poly-Si/SiO_x interface is in those cases bypassed by a second or different etching mechanism. It remains unclear which properties of the poly-Si/SiO_x stack influence the crystallite formation. For example, the different etching mechanisms of Ag and glass frit described earlier can cause anisotropy of etching due to the different crystal orientations in the poly-Si layer.[21] In addition, microstructural analysis with SEM showed that an interface with a thermal oxide can strongly slow down or even stop the etching process of the Ag paste.[15] Since the Ag crystallite size can influence the contact behavior, understanding the Ag crystallite formation is very important to achieve an optimal contact. In the study, we investigate the formation of Ag crystallites by applying SEM and (scanning) transmission electron microscopy ((S)TEM) on a five-layer poly-Si stack separated by native silicon oxides.

Atmospheric Pressure Chemical Vapor Deposition Technique: Amorphous silicon (a-Si) deposition by atmospheric pressure chemical vapor deposition (APCVD) is a high-throughput deposition technique that is promising for implementing passivating contacts in existing solar cell production lines.[22,23] Besides the inline concept, a fundamental technical deviation from other deposition methods is the deposition temperature, which is >650 °C for APCVD coatings.[24] Process temperature of other deposition technologies of a-Si like plasma-enhanced chemical vapor deposition (PECVD) or magnetron sputtering is usually not above 400 °C.[25,26] This temperature difference results in some significant changes in the deposited a-Si layer structure. In particular, the crystallinity and the crystallite size of APCVD a-Si layers after crystallization is rather larger than that of PECVD, low-pressure chemical vapor deposition (LPCVD), or sputtered a-Si which has mostly a crystallite size <20 nm.[24,25] This influences in particular the conductivity, which especially increases with larger crystallites (therefore less grain boundaries, which are mostly limiting the conductivity) and has a much stronger influence on the conductivity than, for example, the doping level.[24,27]

Due to the equipment design of inline APCVD tools, a layer thickness change can be carried out on the one hand by varying the belt speed or on the other hand by multiple drive-through (DT) in the equipment. Using the DT approach, a native oxide grows when the sample cools down under air atmosphere after it passes the deposition section. When passing through again, this intermediate SiO_x ($SiO_{x,inter}$) layer separates the first a-Si layer from the second a-Si layer. At this point, it should be noted that in industrial fabrication, an increase in film thickness with the multiple DT approach will most probably not be achieved by several complete passes of the tool with the attendant cooling of the sample to room temperature, as is the case here with manual handling. Rather, in the deposition zone, several injectors are placed directly behind each other, which means that the automatic formation of a thermal oxide between the two DT would no longer be a consequence. However, if needed, the formation of a thermal oxide between two a-Si layers would be easy to realize by injecting oxide-forming gases.

The authors did not investigate the fabrication of a thin $SiO_{x,inter}$ layer during a-Si deposition using other deposition methods. However, for all CVD-based approaches and sputtering, the implementation of such an interlayer is straightforward. The CVD methods would need an oxygen-providing precursor gas as CO_2 or N_2O besides O_2 while the silane gas is already available for a-Si deposition. Reactive sputtering using a Si target and O_2 can also easily be implemented.

2. Results

2.1. Characteristics of APCVD a-Si Layer

To better demonstrate the contacting behavior of Ag on poly-Si/SiO_x passivating contacts, we prepared a sample with a ≈250 nm-thick a-Si layer fabricated via five DT for the following investigations. The STEM image in **Figure 1**a shows this layer stack at a position where no contact formation occurs. Five individual poly-Si layers with a thickness of ≈55 nm are visible and separated by a thin intermediate $SiO_{x,inter}$ layer. In addition, the a-Si layer consisting of cuboidal blocks with a width of

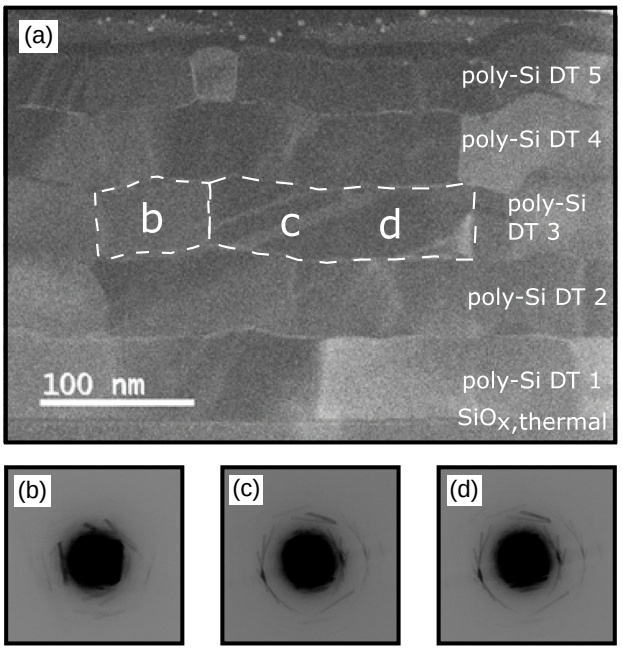

Figure 1. a) High-angle-annular dark field–STEM (HAADF–STEM) image of a layer stack realized with five APCVD DT. b–d) Diffraction images using CBED at positions b, c, and d, respectively, marked in (a). Kikuchi pattern in (c) and (d) are similar and thus show same crystallite orientation, (b) is different to both (see also Figure S1, Supporting Information).

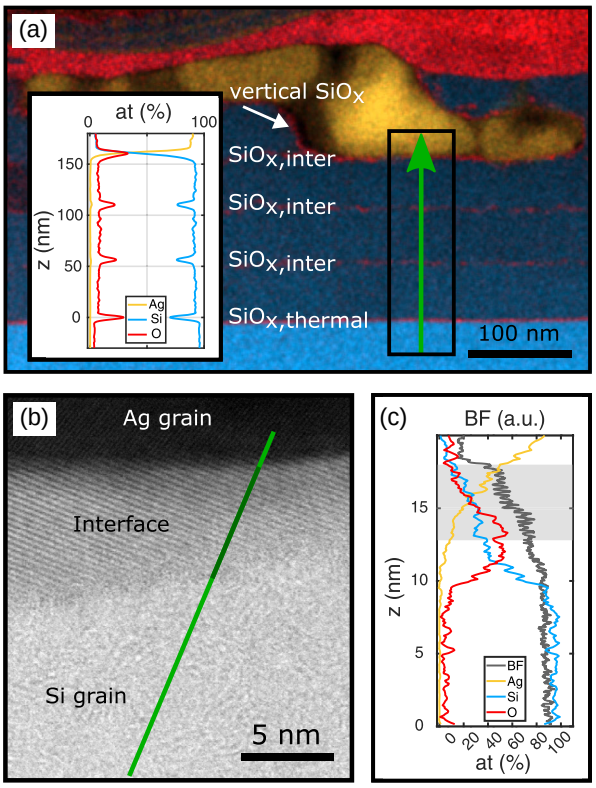

Figure 2. STEM images of a poly-Si layer stack deposited by five APCVD DT. a) EDX map of oxygen (O, red), silicon (Si, blue), and silver (Ag, yellow), where the inset shows a line scan of the highlighted region (green arrow, profile signal averaged in horizontal direction inside the black rectangle). While $SiO_{x,thermal}$ is grown in a controlled process in tube furnace, $SiO_{x,inter}$ forms during cooling after the poly-Si deposition in air atmosphere. The vertical SiO_x is formed during the contact formation process with Ag. b) High-resolution bright-field (BF-STEM) image of the interface between the Ag grain and the underlying Si grain. c) EDX line scan of Ag, O, and Si at the marked line in (b). The line scan of the BF signal indicates a crystalline phase at the interface region between the Ag and Si grain (gray highlighted area).

100–200 nm can be seen. In order to obtain information about the crystal orientation, we analyzed these individual grains via electron diffraction. As an example, the convergent beam electron diffraction (CBED) images are shown in Figure 1b–d. The diffraction image in Figure 1b was taken at position (b) and shows a specific crystal orientation given by the specific arrangement of Kikuchi lines (black, elongated features around the central black spot). Measuring two diffraction patterns at position (c) and (d) in the neighboring block yields the CBED measurements in Figure 1c,d, respectively. It becomes evident that both measurements show the same diffraction pattern indicating that one block consists of single-crystalline Si domains. Measurements at further positions (Supporting Information) also show very clearly that individual blocks always correspond to one Si crystallite. At this point, it should be noted that the crystallite grain size in direct observation by electron microscopy can differ significantly from measurements by X-Ray diffraction (XRD) or Raman measurements.[28] Especially when dealing with complex sample structures and grain sizes in the same order of magnitude as the investigated layer thickness or larger (in this case, particularly wide), common methods are unable in resolving them. As a result, TEM investigations are superior in studying the actual distribution, even though conducting larger experiments may not be feasible by TEM studies.

2.2. Silver Crystallite and SiO_X Formation

In **Figure 2**, the APCVD poly-Si/SiO_x layer stack is shown at a position where a contact with the Ag paste is formed. In Figure 2a, an energy-dispersive X-Ray spectroscopy (EDX) analysis map shows the elemental distribution of oxygen (O, red), silicon (Si, blue), and silver (Ag, yellow). On top of the blue-colored poly-Si layer stack, the red area refers to the glass layer. The yellow-colored Ag crystallites are located within the upper two poly-Si layers. Moreover, the Ag crystallites do not grow arbitrarily deep into the poly-Si layer stack, but always stop at a $SiO_{x,inter}$ layer separating individual poly-Si layers. This stopping behavior between the first and second or second and third poly-Si layers is observed not only here, but at all locations analyzed by the authors. In the horizontal direction, it cannot be ruled out that the Ag crystallites stop at the interface between individual Si grains. The Ag crystallites have a lateral size of up to 400 nm and a height that is thus a multiple of the thickness of the poly-Si layer.

The differently thin SiO_x layers are also apparent in Figure 2a and in the inset, which shows the recording of an EDX line scan. The signal height of the intermediate $SiO_{x,inter}$ layer is lower than that of the thermally grown interface $SiO_{x,thermal}$. This indicates that these $SiO_{x,inter}$ layers are thinner than the 1.5 nm-thick SiO_x,

$_{thermal}$ layer or less dense and thus might have more pinholes for charge carrier transport. Furthermore, whereas in the STEM image in Figure 1, the vertical and horizontal boundaries of a single Si crystallite appear similar, the EDX image indicates that there are no vertical SiO_x regions around the Si crystallites. As the Ag crystallite shown here is embedded in the poly-Si layers with a SiO_x interface layer, the vertical O signal around the Ag crystallite must therefore be a result of the Ag crystallite formation process. By finding a higher oxygen peak at the Ag–Si interface compared to the Si–Si grain interface ($SiO_{x,inter}$) in the inset of Figure 2a, it becomes evident that the oxygen signal is caused by the Ag crystallite formation process. This existence of O is the main difference to the Ag crystallites in classically diffused c-Si, where no O at this interface was observed or could not be detected.[8,11] Taking this investigation further, it follows directly that the theoretical contact formation model between Si and Ag crystallites changes from a Schottky contact to a metal–insulator–semiconductor (MIS) contact. The authors carried out temperature-dependent transfer length method (TLM) measurements from 80 to 350 K on these samples. However, they could not show with various approaches any tunnel-like behavior at this Ag grain/Si grain interface. This may be either because this effect cannot be resolved with standard macroscopic tools or because the charge carrier transport is more complex. Possibly, if the oxide is inhomogeneous or negligibly thick at some positions around the Ag crystallite, charge carrier transport could also be pinhole like at these positions. Besides Ag, O, and Si, the STEM EDX mapping shows no other components of the Ag paste in the poly-Si layer. Figure 2b shows the interface between the Ag crystallite and the underlying Si crystallite in lattice resolution. The transition area between the two crystallites is about 5 nm wide. It can be assumed that this width originates from the fact that the contact surface between Ag and Si crystallite is tilted to the zone axis. Figure 2c shows an EDX line scan at the contact area marked in Figure 2b. In addition to the Ag, O, and Si signals, the signal from the BF image can also be seen there. Due to the lattice resolution, this interface region can be clearly identified. The Ag signal, which falls off linearly for the most part in the interface, may indicate also that there is a tilting of the interface between Ag and Si crystallites. Furthermore, due to the intensity of the O signal, it can be assumed that O rather accumulates in the Si layer to SiO_x than at the Ag crystallite.

2.3. Stopping of Silver Crystallite at Poly-Si/SiO_x Interface

This section deals with the abrupt stopping of the Ag paste etching process and the resulting stop of the Ag crystals at poly-Si/SiO_x interfaces. This stop is present not only in a sample with a fivefold poly-Si layer, but also in a sample with an 80 nm poly-Si/$SiO_{x,thermal}$ layer stack from a single DT (Sample B). **Figure 3**a displays this sample in an ion-milled SEM cross section. Ag crystallites are visible only in the poly-Si layer and are separated by a glass layer from the Ag bulk. The Ag crystallites have in parts a rectangular shape and stop at the interface of the $SiO_{x,thermal}$ layer, which makes this stopping behavior comparable to the sample with the fivefold DT. This raises the question of why the formation of Ag crystallites is stopped at the interface with a SiO_x layer.

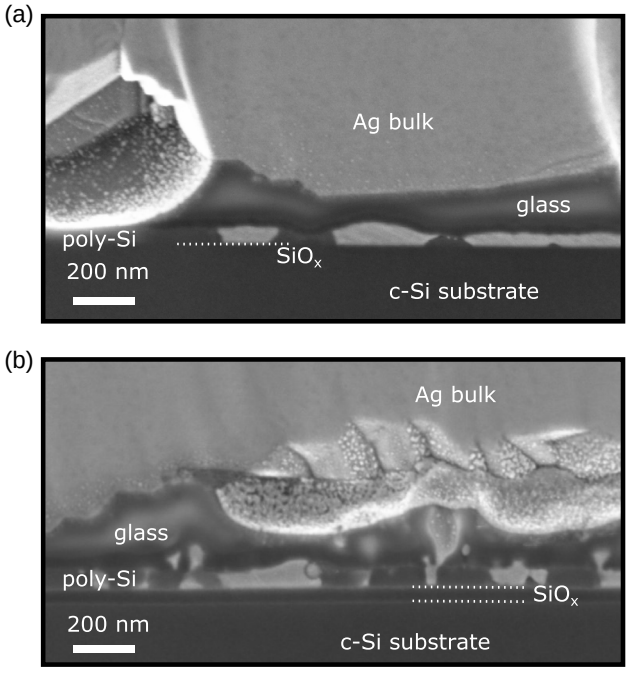

Figure 3. SEM images of the cross section of a passivating contact with a single DT (*n*) poly-Si layer. a) Sample B with thin thermal oxide of 1.5 nm and b) Sample C with a thick thermal oxide of >50 nm.

A first explanation is that the presence of the SiO_x layer forms a barrier to the etching reaction (*I*) of Ag. This view is supported, in particular, by a sample on which the 80 nm-thick poly-Si layer is deposited on a ≈50 nm-thick-grown SiO_x layer (Sample C in Figure 3b). Again, the Ag crystallites exclusively grow in the poly-Si layer. The Ag crystallites clearly stop above the SiO_x while etching of the SiO_x layer is not observed.

Another possible explanation for the observed stop of Ag crystallite growth is the change in crystal orientation at the interfaces. At the firing temperature of ≈800 °C, the Ag paste etching mechanism can be seen as a solution of Si in Ag according to reaction (1). It was observed that the etching process of the {111} crystal planes is slower than that of {100} planes, leading mainly to inverted pyramids when classical, diffused (100) c-Si samples are contacted.[10,29] However, contact formation experiments on planar samples with {111}-oriented surfaces showed no direct etch stop, but lens-shaped Ag crystallites.[10,30] A complete etch stop at the interface to an {111}-oriented Si crystallite is thus hardly conceivable. However, the crystal orientation of the respective Si crystallites will still have an influence on the etching behavior.

In order to look for possible correlations, we determine in the following the crystal orientation of two different Ag crystallites and their immediately neighboring Si crystallites. On the one hand, as in the classical case of contacted c-Si, we may find that the Ag crystallites have a fixed crystal orientation with respect to the Si surface due to the epitaxial growth there.[11,12] On the other hand, Si grains with {111}-oriented planes could face the Ag crystallite and thus may explain a slowed-down etching reaction in this Si grain. However, due to the quasi-2D structure of the

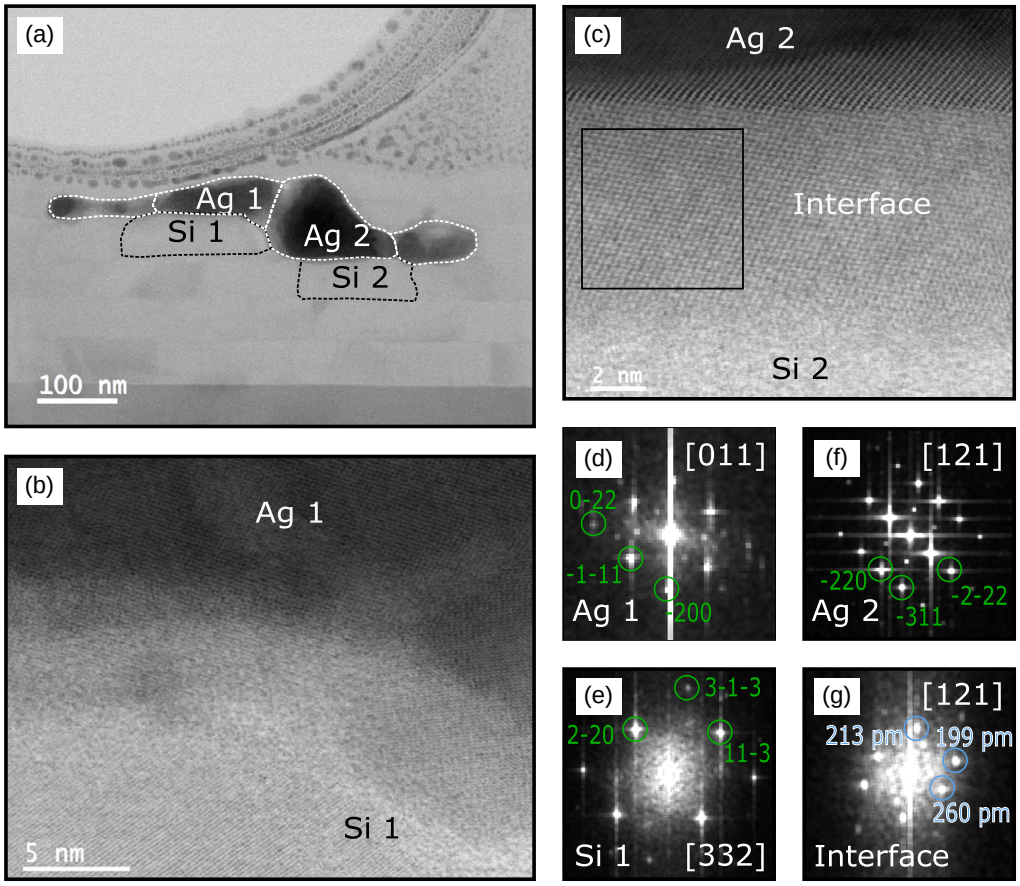

Figure 4. STEM images of a layer stack with five DT deposition. a) All Ag grains with different crystal orientations are marked as well as exemplarily two neighboring Si grains. b) Interface between grain Ag 1 and grain Si 1 where the sample is oriented in zone axis [332] of the Si 1 grain. c) Interface between grain Ag 2 and Si 2, where the sample is oriented in Ag-zone axis [121]. d) Diffraction pattern (FFT) of Ag 1 grain, while sample tilted was tilted in zone axis [011] of Ag 1 grain. e) FFT of Si 1 grain recorded when the sample is tilted as in (b). f,g) FFT patterns of the Ag 2-Si 2 interface, respectively, while the sample was tilted in the zone axis [121] of the Ag grain as in (c).

TEM lamella, only parts of all possible correlations between the Ag crystallite and the Si neighboring crystallites can be found.

Using CBED diffraction studies, we have determined individual grains of both the Ag crystal and the Si layers in **Figure 4**a. The Ag crystal is segmented into four different individual crystallites. The orientation of the two marked grains (Ag 1 and Ag 2) and the underlying Si crystallites (Si 1 and Si 2) has been determined as follows. First, the sample was tilted to the next available low-order zone axis using Kikuchi lines within the CBED diffraction pattern. Second, high-resolution STEM images of the crystallites were acquired and from the corresponding fast-Fourier-transform (FFT) images (Figure 4d–g) the zone axis was identified using CrysTBox toolbox.[31,32] For the Ag 1 crystallite, the zone axis was determined as [011] (Figure 4d). The Bragg reflex in the direction of the Si 1 crystallite indicates that the Ag 1 crystal orientation toward this Si 1 crystallite has a (200) surface. Next, the sample was further tilted to get into the [332] zone axis for the Si 1 crystallite. In this tilted state, a high-resolution TEM image of the interface between the Ag 1 and Si 1 crystallites is shown in Figure 4b. An FFT image in the Si region (Figure 4e) shows that there is no low-order crystal orientation in the direct direction of the Ag 1 crystallite. The closest assignable plane according to the FFT image is the (3–1–3) plane.

The same investigation is performed for the Ag 2 and Si 2 grains. While the zone axis [121] can be detected for the Ag 2 grain, tilting of the sample into a low-order zone axis of the Si 2 grain was not possible (the required tilt angle could not be reached because of the limited tilt range of the sample holder). If the sample is tilted in a way that Ag 2 is in this [121] zone axis, Figure 4c is obtained. The Bragg reflexes in Figure 4f show that the Ag plane which is facing the Si 2 grain surface is the (-311) plane. It is also noticeable that the interface between Ag and Si is very wide (same interface as in Figure 2). This indicates that the interface between the Ag and the Si crystallite may be slightly tilted and thus overlap each other. An FFT image of the interface (Figure 4g) shows that in addition to the Ag reflections, which can still be seen very lightly, there are other reflections, probably from an interface layer. The Bragg reflexes marked in blue are different from those of the Ag 2 crystallite. Since it was not possible to assign them to a Si or any other Ag crystallite orientation, we assume that the etching process could form a crystalline phase of Ag, Si, and O. A detailed investigation of this interface may be the subject of further research.

Referring back to the origin of the Ag crystallites stop at these interfaces, we can exclude that the Si grain has a direct (111) plane to the Ag for both interfaces. Moreover, no fixed phase relationships between Ag and Si are observed at the investigated sites.

In addition, the FFT image can be used to determine the angle to the nearest (111) plane. As shown in Figure 4e, for example, the planes (11-3) and (2-20) are orthogonal to the zone axis (332). With their orientation and by help of CrystTBox, the plane in the interface between the Ag and Si crystallites was determined to (4-2-3).[31,32] Since this plane is tilted only by 15.2° from the (1-1-1) plane, the etch rate of Ag into the poly-Si may be significantly reduced. However, a complete etch stop would only occur by chance since the etching rate is only reduced for this Si plane. If the different etch rates were the dominant effect for this stopping mechanism, it would be more likely that the Ag crystallites would generally end at {111} planes, also within individual Si grains. Additionally, differently shaped Ag crystallites, such as inverted pyramids, should also be visible in the cross-sectional view. Nevertheless, we observe that all Ag crystallites always stop at the interfaces of the poly-Si layers and never within a Si grain, which also defines the cuboidal shape of the Ag crystallites.

In summary, the etching of the Ag paste into the poly-Si layer stack can certainly be influenced by the orientation of the neighboring Si crystallites. However, since Ag dissolves some crystal planes more slowly and Ag etching never leads to a complete etch stop, we suspect that the interface itself, and in particular the presence of the grown silicon oxide, can greatly reduce the etch reaction (1), which then leads to this abrupt stop of Ag crystallite at the interface with the $SiO_{x,inter}$.

2.4. Oxide Layer Around Silver Crystallite

The second fundamental difference in Ag crystallite formation for APCVD-based passivating contacts compared to diffused junctions is the appearance of the SiO_x layer around the Ag crystallites. In addition to the consequences for current transport already mentioned above, the question of formation is of particular interest. Since an in situ observation of the etching process at ≈800 °C is technically difficult to realize, a precise reaction determination is only possible indirectly via the sample's status after this contact formation process.

The studies of the interface with Ag crystallite formation in c-Si already indicate very clearly that there is no oxide around the Ag crystallites, although the technical possibilities were probably less developed.[8,11] We identify the following explanations for the formation of the SiO_x layer around the Ag crystallites in passivating contacts. A first mechanism may be caused by the difference in thermal expansion of Ag and Si. While Ag has an expansion coefficient at 20 °C of 18.9 μm m $^{-1}$ K $^{-1}$, that of Si is only 2.6 μm m $^{-1}$ K $^{-1}$ at 20 °C.[33,34] Consequently, also at higher temperatures, thermal stress must occur between Ag and Si due to the different coefficients of expansion. This can lead to stress between Ag and Si when cooling below the softening point where recrystallization of Ag takes place. However, the question remains as to why this effect does not occur in the formation of Ag crystallites in a c-Si substrate. We therefore assume that this effect is not responsible for the formation of the oxides around the Ag crystallite.

The following two explanations seem to be more feasible. Based on the studies earlier on the crystal orientations of Ag and Si and the corresponding interface in particular, no fixed correlation between the two crystal lattices was observed. In contrast to Ag crystallites in c-Si, it is never possible for Ag to grow with an epitaxial relationship on all Si interfaces due to the different orientation of all neighboring Si crystallites. Nevertheless, it can be assumed that the Ag crystallite growth starts epitaxially at one Si crystallite. In this case, there is a high probability of a mismatch with all other neighboring Si crystallites. At those other contact interfaces, stress, vacancies, or other crystal defects are inevitably formed, facilitating the incorporation of O from the glass layer or the atmosphere. By implication, however, this would also mean that at least one interface to a poly-Si crystallite does not have an intermediate layer of SiO_x for each Ag crystallite and has an epitaxial relationship between the corresponding Ag and Si crystallites. The investigation did not find evidence of the epitaxial relationship between Ag and Si crystallites in this TEM lamella. However, due to the 3D nature of the Ag crystallites within the poly-Si layer, this cannot be completely ruled out. Alternatively, the recrystallization of Ag in the present case could also start from a random position in the softened Ag phase during cool down at the end of the firing process. In this case, Ag would most likely encounter an arbitrarily oriented Si surface, whereby no lattice matching between Ag and Si would be possible. The surface of the Ag crystallite and the Si grain then may oxidize and a disordered interface layer with a high oxygen content would be formed.

2.5. Application of Multilayer Approach in Solar Cells

The multilayer approach of the poly-Si layer with multiple a-Si DTs, as presented, can be a viable concept for improving passivation quality under metal contacts in solar cell applications. The main idea is to create a controllable barrier for Ag crystallites, preventing them from being in direct contact with the c-Si substrate and thus causing highly recombination active defects at the c-Si surface. To validate this DT approach, we prepared samples with different metallized areas to determine the metal saturation current density ($J_{0,Met}$). The processing and characterization of these samples was conducted along with the samples previously published in ref.[15] (Sample group C), where fabrication and characterization details can be found.

To investigate the effect of the multilayer approach, we prepared three different sample groups: one group with a single poly-Si layer of 50 nm thickness and two groups with a multilayer stack with a total poly-Si layer thickness of 150 nm. The two multilayer groups differ in the number of DTs: the first group contains 5 DTs with single-layer thickness of 30 nm, while the second group contains 3 DTs with a single poly-Si layer thickness of 50 nm. Note that as the number of DTs increases, the number of SiO_x interlayers increases accordingly. Thus, although the 3-DT samples may have some Ag crystallites reaching the $SiO_{x,thermal}$ interface, this is impossible for the 5-DT samples, although their total poly-Si thickness is comparable.

By analyzing the results shown in **Figure 5**a, it can be observed that all sample groups achieve low contact resistivities (ρ_C) in the range of 3–10 mΩ cm^2 at the highest set peak firing temperature.

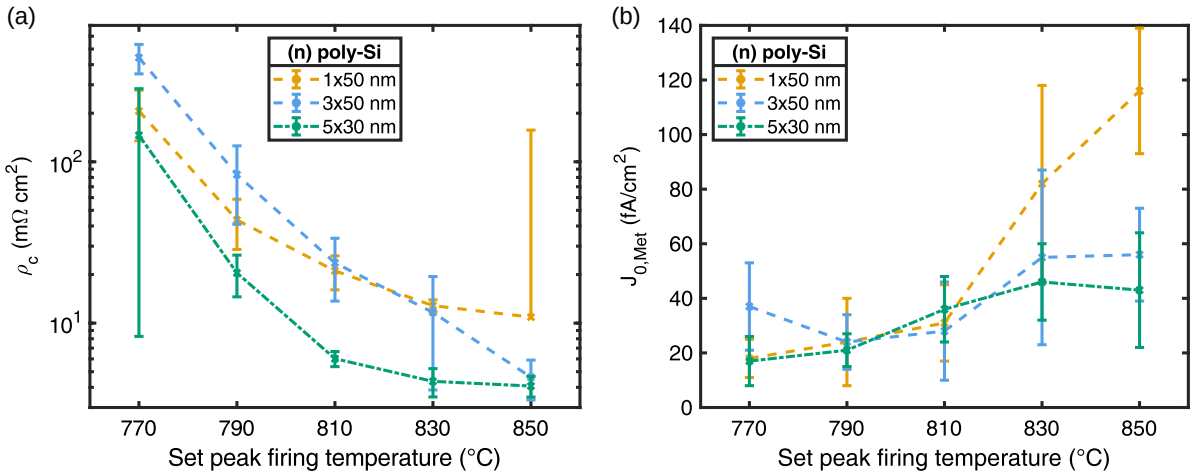

Figure 5. Solar cell parameters for multilayer poly-Si stack with different DTs integrated in precursor samples fired at different set peak firing temperatures. a) Contact resistivity (ρ_C) and b) saturation current density at the metallized areas ($J_{0,Met}$).

Specifically, the 150 nm-thick films tend to achieve the lowest ρ_C values, and more DTs could be advantageous since lower set peak firing temperatures can achieve low ρ_C. On the other hand, $J_{0,Met}$ of the single-DT samples is higher than that of the multilayer samples, remaining below ≈60 fA cm^{-2}, as shown in Figure 5b. Despite the relatively high uncertainty of the data presented in this study, there is a possibility that the five DT samples could have slightly lower $J_{0,Met}$ values compared to the three DT sample. The authors estimate that this effect may become more statistically significant in a study with a larger sample size. Furthermore, besides the more favorable solar cell parameters achieved with the multilayer approach, the integration of the $SiO_{x,inter}$ interlayer into the poly-Si has the potential to enhance precise control of Ag crystallite size and formation. This improvement could prove advantageous in industrial manufacturing processes.

As discussed earlier, APCVD a-Si has a larger grain size compared to other deposition technologies. However, in a study[35] varying several process parameters for Ag contact formation on poly-Si/SiO_x passivation contacts, the authors could not find any fundamental difference for different deposition techniques, in particular for PECVD and APCVD (n) poly-Si layers. In general, an influence of the poly-Si crystallite size and orientation on contact formation and thus on solar cell performance could, besides the here-performed TEM investigation, also not be resolved with macroscopic examination methods in other experiments.

3. Conclusion

We have investigated the formation of Ag crystallites in poly-Si/SiO_x passivating contacts. Overall, the Ag paste applied shows similar etching reactions on passivating contacts as have been widely studied on classically, diffused c-Si. Here, the focus was on the Ag crystallite formation, which enables direct metal–semiconductor contacts. However, the shape and position of these Ag crystallites grown into the poly-Si layer are very different from that in classical c-Si contact formation. The crystallites are always located in poly-Si layers and stop at the underlying SiO_x interfaces. The $SiO_{x,inter}$ layers formed during APCVD a-Si deposition seem to play a more dominant role than the crystal orientation of the underlying silicon. This barrier effect can now also be used as a barrier layer for Ag crystallite formation. Thus, it could be shown that the contact resistivity is lower and the passivation quality is higher for the multilayer concept than for the single poly-Si layer. Comparable thick poly-Si layers with three and five DT indicate that the integration of more $SiO_{x,inter}$ layers results in lower ρ_C and possibly also in better surface passivation. A second key finding is the presence of an oxide layer around the grown Ag crystal. This is presumably formed during cooling within the firing process and the result of a missing correlation between the neighboring Ag and Si crystallites. Consequently, the contact resistance between poly-Si and Ag crystallites must be described, for example, via an MIS contact or only locally allowed transport and then with current crowding effects. This makes the formation of Ag crystallites in poly-Si passivating contacts significantly different from cell concepts based on classically diffused c-Si.

4. Experimental Section

Sample Preparation and Precharacterization: Czochralski (Cz)-grown n-type-doped (4.5 Ω cm) crystalline silicon wafers in M2 size and a thickness of 150 µm were saw damage etched in potassium hydroxide and afterward cleaned with a wet chemical ozone and piranha cleaning. While a 1.5 nm-thick thermal oxide was grown in a conventional tube furnace for Samples A and B, 50 nm thermal oxide was grown for Sample C. Phosphorous-doped poly-Si was deposited with APCVD tool at T > 650 °C. For Samples B and C, a single layer with a thickness of ≈80 nm was deposited. For Sample A, five of these single layers were deposited sequentially, resulting in a total layer thickness of ≈270 nm. Subsequently, a wet chemical ozone cleaning was done, before the samples were crystallized in a tube furnace for 30 min at 920 °C in N_2 atmosphere. For hydrogenation of the passivating contact in the fast firing step, first a 75 nm-thick SiN_x layer was deposited on both sides using a PECVD tool. For metallization, a lead-free Ag paste comparable to commercial pastes was applied with standard screen-printing technique. After a drying process, the contact formation was

performed in a conventional fast firing belt furnace at a measured sample peak firing temperature of ≈825 °C. For Sample A, an implied open-circuit voltage (iV_{OC}) of 742 mV was obtained using (photoconductance decay) PCD measurement with a Sinton lifetime tester WCT-120 after SiN_x deposition, but prior to metallization and fast firing. After metallization, a contact resistivity (ρ_C) of 1.8(11) mΩ cm^2 was determined on the same sample utilizing a PV tools TLM setup.

A different sample batch was used to evaluate the effect of the multilayer stack on the solar cell parameters. In addition to the infeasibility of $J_{0,Met}$ evaluation with the TLM metallization pattern used for Samples A, B, and C, the base resistivity of those three samples prevents proper evaluation of $J_{0,Met}$ values under high injection conditions. For a comprehensive description of the fabrication and characterization of the samples presented in Section 2.5, please refer to ref.[15] (Sample group C).

TEM Sample Preparation Using Focused Ion Beam (FIB): For the TEM sample preparation, we used a ThermoFisher Helios NanoLab G3 FIB-SEM DualBeam system. It provides gallium ions with energies up to 30 keV. We prepared the sample in the zone axis [110] of the Si substrate as a reference. Taking into account the sample structure and the region of interest located between the Si substrate and the Ag contact, we preferred to perform the nonstandard upside-down ion-milling procedure, that is, with an ion-milling direction from the Si substrate to the Ag contact,[36] in order to ensure more homogeneous milling rates and to prevent curtaining artifacts due to the existing voids/cavities in the Ag contact. **Figure 6** shows the principle of this technique. We finalized the preparation with low ion-energy steps at 5 and 2 keV, respectively, minimizing the damage layer on the lamella side walls and achieving an estimated lamella thickness in the range of 25–40 nm at the poly-Si/SiO_x stack.

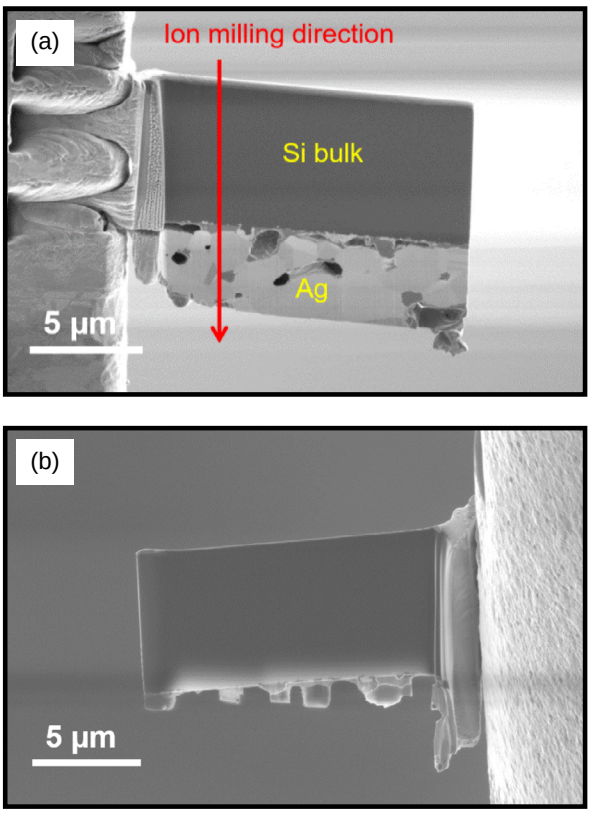

Figure 6. SEM images showing the TEM sample. a) FIB preparation with the upside-down technique. b) Final TEM lamella with a thickness of 25–40 nm.

Measurements: The contact interface between the Ag finger and the poly-Si/SiO_x structure was investigated by SEM in cross-section view after ion milling. Atomic structure resolution of the interface was achieved by high resolution TEM. STEM was applied in combination with EDX in two different TEMs, an aberration-corrected Jeol ARM 200 F (probe and image corrected, for atomic-resolved imaging, Figure 1, 2(b)+(c) and 4) and a Thermo Fisher Scientific Talos 200 F (equipped with 4 SDD EDX detectors, for EDX mapping, Figure 2a). The electron beam energy was for both microscopes 200 keV and the beam current ranged between 50 and 350 pA. The point resolutions of the microscopes were 0.8 Å (ARM) and 1.6 Å (Talos), respectively. To achieve sufficient signal-to-noise ratio in case of EDX measurement (Figure 2a), the multiple frame approach was applied, which means that the electron beam was scanned across the region of interest (≈600 × 900 pixel) 150 times, with an acquisition time of 20 µs and a scanning step size of 500 pm per pixel. The signal was integrated later over all frames. To compensate for sample drift during EDX acquisition, online drift correction was applied by cross-correlation after each frame. To verify the resolution capabilities of the Jeol ARM microscope, Si dumbbells (136 pm) on the Si substrate could be clearly resolved by imaging (HAADF and BF) and a simultaneously measured EDX line profile. The crystal structure and orientation analysis in Figure 4d–g was done using CrysTBox Server 1.0.[31,32]

Supporting Information

Supporting Information is available from the Wiley Online Library or from the author.

Acknowledgements

This work was partially funded by the German Federal Ministry for Economic Affairs and Climate Action under contract number 03EE1022C (project FUN) and by the Netherlands under the Dutch contract no. SOL18004 both within the solar-era net. F.P.S., A.H., and T.L. acknowledge the German Federal Ministry for Education and Research (BMBF) under the grants Catlab (03EW0015B) and e-conversion (390776260) for funding. T.L. acknowledges funding by the Deutsche Forschungsgemeinschaft (DFG, German Research Foundation) under Germany's Excellence Strategy-EXC2089/1-390776260. The content is the responsibility of the authors.

Open Access funding enabled and organized by Projekt DEAL.

Conflict of Interest

The authors declare no conflict of interest.

Data Availability Statement

The data that support the findings of this study are available from the corresponding author upon reasonable request.

Keywords

Ag pastes, metallization, passivating contacts, poly-Si, stopping, transmission electron microscopy

Received: June 28, 2023
Revised: August 29, 2023
Published online: September 12, 2023

[1] A. Richter, R. Müller, J. Benick, F. Feldmann, B. Steinhauser, C. Reichel, A. Fell, M. Bivour, M. Hermle, S. W. Glunz, *Nat. Energy* **2021**, *6*, 429.
[2] M. A. Green, E. Dunlop, M. Yoshita, N. Kopidakis, K. Bothe, G. Siefer, X. Hao, *Prog. Photovolt.* **2023**, *31*, 651.
[3] F. Haase, C. Hollemann, S. Schäfer, A. Merkle, M. Rienäcker, J. Krügener, R. Brendel, R. Peibst, *Sol. Energy Mater. Sol. Cells* **2018**, *186*, 184.
[4] VDMA, International Technology Roadmap for Photovoltaic 2022 Results, https://www.vdma.org/international-technology-roadmap-photovoltaic, **2023**.
[5] G. Schubert, F. Huster, P. Fath, *Sol. Energy Mater. Sol. Cells* **2006**, *90*, 3399.
[6] K.-K. Hong, S.-B. Cho, J. S. You, J.-W. Jeong, S.-M. Bea, J.-Y. Huh, *Sol. Energy Mater. Sol. Cells* **2009**, *93*, 898.
[7] J. D. Fields, M. Ahmad, V. L. Pool, J. Yu, D. G. Van Campen, P. A. Parilla, M. F. Toney, M. F. Van Hest, *Nat. Commun.* **2016**, *7*, 11143.
[8] C. Ballif, D. Huljić, G. Willeke, A. Hessler-Wyser, *Appl. Phy. Lett.* **2003**, *82*, 1878.
[9] E. Cabrera, S. Olibet, J. Glatz-Reichenbach, R. Kopecek, D. Reinke, G. Schubert, *J. Appl. Phys.* **2011**, *110*, 114511.
[10] G. Schubert, *Doctoral Dissertation*, University of Konstanz, Konstanz **2006**.
[11] M.-I. Jeong, S.-E. Park, D.-H. Kim, J.-S. Lee, Y.-C. Park, K.-S. Ahn, C.-J. Choi, *J. Electrochem. Soc.* **2010**, *157*, H934.
[12] K. T. Butler, P. E. Vullum, A. M. Muggerud, E. Cabrera, J. H. Harding, *Phys. Rev. B* **2011**, *83*, 235307.
[13] C.-H. Lin, S.-Y. Tsai, S.-P. Hsu, M.-H. Hsieh, *Sol. Energy Mater. Sol. Cells* **2008**, *92*, 1011.
[14] K. Ren, D. Han, T. Ye, Y. Zhang, A. Ebong, *J. Appl. Phys.* **2020**, *127*, 225302.
[15] R. Glatthaar, F. Huster, T. Okker, B. Cela Greven, S. Seren, G. Hahn, B. Terheiden, *Phys. Status Solidi A* **2022**, *219*, 2200501.
[16] A. Chaudhary, J. Hoß, J. Lossen, F. Huster, R. Kopecek, R. van Swaaij, M. Zeman, *Phys. Status Solidi A* **2021**, *218*, 2100243.
[17] P. Padhamnath, A. Khanna, N. Nandakumar, A. G. Aberle, S. Duttagupta, *Sol. Energy Mater. Sol. Cells* **2021**, *230*, 111217.
[18] R. Peibst, F. Haase, B. Min, C. Hollemann, T. Brendemühl, K. Bothe, R. Brendel, *Prog. Photovolt.* **2022**, *31*, 327.
[19] H. E. Çiftpınar, M. K. Stodolny, Y. Wu, G. J. Janssen, J. Löffler, J. Schmitz, M. Lenes, J.-M. Luchies, L. Geerligs, *Energy Procedia* **2017**, *124*, 851.
[20] P. Padhamnath, N. Nampalli, A. Khanna, B. Nagarajan, A. G. Aberle, S. Duttagupta, *Sol. Ener.* **2022**, *231*, 8.
[21] G. C. Cheek, R. P. Mertens, R. Van Overstraeten, L. Frisson, *IEEE Trans. Electron Devices* **1984**, *31*, 602.
[22] B. Kafle, B. S. Goraya, S. Mack, F. Feldmann, S. Nold, J. Rentsch, *Sol. Energy Mater. Sol. Cells* **2021**, *227*, 111100.
[23] A. Merkle, S. Seren, H. Knauss, B. Min, J. Steffens, B. Terheiden, R. Brendel, R. Peibst, in *35th EUPVSEC*, Marseille **2018**, pp. 785–791.
[24] J. F. Mousumi, G. Gregory, J. P. Ganesan, C. Nunez, K. Provancha, S. Seren, H. Zunft, T. Jurca, P. Banerjee, A. Kar, *Phys. Status Solidi RRL* **2022**, *16*, 2100639.
[25] T. N. Truong, D. Yan, C. P. T. Nguyen, T. Kho, H. Guthrey, J. Seidel, M. Al-Jassim, A. Cuevas, D. Macdonald, H. T. Nguyen, *Prog. Photovolt.* **2021**, *29*, 857.
[26] J. Linke, S. Weit, J. Rinder, R. Glatthaar, S. Möller, G. Hahn, B. Terheiden, *IEEE J. Photovolt.* **2020**, *10*, 1624.
[27] T. Okker, R. Glatthaar, F. Huster, S. Seren, G. Hahn, B. Terheiden, in *SiliconPV 12*, Konstanz **2022**.
[28] C. Weidenthaler, *Nanoscale* **2011**, *3*, 792.
[29] D. Pysch, A. Mette, A. Filipovic, S. Glunz, *Prog. Photovolt.* **2009**, *17*, 101.
[30] P. Kumar, M. Pfeffer, B. Willsch, O. Eibl, *Sol. Energy Mater. Sol. Cells* **2016**, *145*, 358.
[31] M. Klinger, *CrysTBox-Crystallographic Toolbox*, Institute of Physics of the Czech Academy of Sciences, Prague **2015**.
[32] M. Klinger, *J. Appl. Crystallogr.* **2017**, *50*, 1226.
[33] W. M. Haynes, *CRC Handbook of Chemistry and Physics*, CRC Press, Taylor & Francis Group, Boca Raton, FL **2016**.
[34] H. Watanabe, N. Yamada, M. Okaji, *Int. J. Thermophys.* **2004**, *25*, 221.
[35] R. Glatthaar, B. Cela Greven, T. Okker, F. Huster, G. Hahn, B. Terheiden, *Sol. Energy Mater. Sol. Cells* **2023**, *261*, 112516.
[36] D. Abou-Ras, U. Bloeck, S. Caicedo-Dávila, A. Eljarrat, H. Funk, A. Hammud, S. Thomas, D. R. Wargulski, T. Lunkenbein, C. T. Koch, *J. Appl. Phys.* **2023**, *133*, 121101.